arXiv:1202.1829v2 [astro-ph.CO] 4 May 2012

A COMPREHENSIVE VIEW OF A STRONGLY LENSED PLANCK-ASSOCIATED SUBMILLIMETER GALAXY

Hai Fu[1], E. Jullo[2], A. Cooray[1], R.S. Bussmann[3], R.J. Ivison[4], I. Pérez-Fournon[5,6], S.G. Djorgovski[7,8], N. Scoville[7], L. Yan[7], D.A. Riechers[7], J. Aguirre[9], R. Auld[10], M. Baes[11], A.J. Baker[12], M. Bradford[7], A. Cava[13], D.L. Clements[14], H. Dannerbauer[15,16], A. Dariush[17], G. De Zotti[18,19], H. Dole[20], L. Dunne[21], S. Dye[21], S. Eales[10], D. Frayer[22], R. Gavazzi[23], M. Gurwell[3], A.I. Harris[24], D. Herranz[25], R. Hopwood[17], C. Hoyos[21], E. Ibar[4], M.J. Jarvis[26,27], S. Kim[1], L. Leeuw[28,29], R. Lupu[9], S. Maddox[21], P. Martínez-Navajas[6,5], M.J. Michałowski[30], M. Negrello[18,31], A. Omont[23], M. Rosenman[9], D. Scott[32], S. Serjeant[31] I. Smail[33], A.M. Swinbank[33], E. Valiante[10], A. Verma[34], J. Vieira[7], J.L. Wardlow[1], P. van der Werf[35]

ApJ accepted

ABSTRACT

We present high-resolution maps of stars, dust, and molecular gas in a strongly lensed submillimeter galaxy (SMG) at $z = 3.259$. HATLAS J114637.9−001132 is selected from the *Herschel*-Astrophysical Terahertz Large Area Survey (H-ATLAS) as a strong lens candidate mainly based on its unusually high 500 μm flux density (∼300 mJy). It is the only high-redshift *Planck* detection in the 130 deg^2 H-ATLAS Phase-I area. Keck Adaptive Optics images reveal a quadruply imaged galaxy in the K-band while the Submillimeter Array and the Jansky Very Large Array show doubly imaged 880 μm and CO(1→0) sources, indicating differentiated distributions of the various components in the galaxy. In the source plane, the stars reside in three major kpc-scale clumps extended over ∼1.6 kpc, the dust in a compact (∼1 kpc) region ∼3 kpc north of the stars, and the cold molecular gas in an extended (∼7 kpc) disk ∼5 kpc northeast of the stars. The emission from the stars, dust, and gas are magnified by ∼17, ∼8, and ∼7 times, respectively, by four lensing galaxies at $z \sim 1$. Intrinsically, the lensed galaxy is a warm ($T_{\rm dust} \sim 40-65$ K), hyper-luminous ($L_{\rm IR} \sim 1.7 \times 10^{13}$ L$_\odot$; SFR ∼ 2000 M$_\odot$ yr^{-1}), gas-rich ($M_{\rm gas}/M_{\rm baryon} \sim 70\%$), young ($M_{\rm stellar}/{\rm SFR} \sim 20$ Myr), and short-lived ($M_{\rm gas}/{\rm SFR} \sim 40$ Myr) starburst. With physical properties similar to unlensed $z > 2$ SMGs, HATLAS J114637.9−001132 offers a detailed view of a typical SMG through a powerful cosmic microscope.

Subject headings: galaxies: formation — galaxies: individual (HATLAS J114637.9−001132) — galaxies: interactions

[1] Department of Physics & Astronomy, University of California, Irvine, CA 92697; haif@uci.edu

[2] Observatoire d'Astrophysique de Marseille-Provence, 38 rue Frédéric Joliot-Curie, F-13388 Marseille, France

[3] Harvard-Smithsonian Center for Astrophysics, 60 Garden Street, Cambridge, MA 02138

[4] UK Astronomy Technology Centre, Royal Observatory, Edinburgh, EH9 3HJ, UK

[5] Instituto de Astrofísica de Canarias (IAC), E-38200 La Laguna, Tenerife, Spain

[6] Departamento de Astrofísica, Universidad de La Laguna (ULL), E-38205 La Laguna, Tenerife, Spain

[7] California Institute of Technology, 1200 E. California Blvd., Pasadena, CA 91125

[8] Distinguished Visiting Professor, King Abdulaziz Univ., Jeddah, Saudi Arabia

[9] Department of Physics and Astronomy, University of Pennsylvania, Philadelphia, PA 19104

[10] School of Physics and Astronomy, Cardiff University, The Parade, Cardiff, CF24 3AA, UK

[11] Sterrenkundig Observatorium, Universiteit Gent, Krijgslaan 281 S9, B-9000 Gent, Belgium

[12] Department of Physics and Astronomy, Rutgers, The State University of New Jersey, 136 Frelinghuysen Rd, Piscataway, NJ 08854

[13] Departamento de Astrofísica, Facultad de CC. Físicas, Universidad Complutense de Madrid, E-28040 Madrid, Spain

[14] Astrophysics Group, Imperial College London, Blackett Laboratory, Prince Consort Road, London SW7 2AZ, UK

[15] Universität Wien, Institut für Astronomie, Türkenschanzstraße 17, 1160 Wien, Österreich

[16] Laboratoire AIM-Paris-Saclay, CEA/DSM-CNRS-Université Paris Diderot, Irfu/SAp, CEA-Saclay, 91191 Gif-sur-Yvette Cedex, France

[17] Physics Department, Imperial College London, Prince Consort Road, London SW7 2AZ, UK

[18] INAF - Osservatorio Astronomico di Padova, Vicolo dell'Osservatorio 5, I-35122 Padova, Italy

[19] SISSA, Via Bonomea 265, I-34136, Trieste, Italy

[20] Institut d'Astrophysique Spatiale (IAS), bâtiment 121, Université Paris-Sud 11 and CNRS (UMR 8617), 91405 Orsay, France

[21] School of Physics and Astronomy, University of Nottingham, NG7 2RD, UK

[22] NRAO, PO Box 2, Green Bank, WV 24944

[23] Institut d'Astrophysique de Paris, UMR 7095, CNRS, UPMC Univ. Paris 06, 98bis boulevard Arago, F-75014 Paris, France

[24] Department of Astronomy, University of Maryland, College Park, MD 20742-2421

[25] Instituto de Física de Cantabria (CSIC-UC), Avda. los Castros s/n, 39005 Santander, Spain

[26] Centre for Astrophysics Research, Science & Technology Research Institute, University of Hertfordshire, Hatfield, Herts, AL10 9AB, UK

[27] Physics Department, University of the Western Cape, Cape Town, 7535, South Africa

[28] Physics Department, University of Johannesburg, P.O. Box 524, Auckland Park, 2006, South Africa

[29] SETI Institute, 189 Bernardo Ave, Mountain View, CA, 94043

[30] Institute for Astronomy, University of Edinburgh, Royal Observatory, Blackford Hill, Edinburgh EH9 3HJ, UK

[31] Department of Physical Sciences, The Open University, Walton Hall, MK7 6AA Milton Keynes, UK

[32] Department of Physics & Astronomy, 325-6224 Agricultural Road, University of British Columbia, Vancouver, BC V6T 1Z1, Canada

[33] Institute for Computational Cosmology, Durham University, Durham DH1 3LE, UK

[34] University of Oxford, Oxford Astrophysics, Denys Wilkinson Building, Keble Road, Oxford, OX1 3RH, UK

[35] Leiden Observatory, Leiden University, P.O. Box 9513, NL-2300 RA Leiden, The Netherlands

1. INTRODUCTION

Bright submillimeter-selected galaxies (SMGs Blain et al. 2002) provide a powerful probe into the distant Universe. Thanks to the negative K-correction in the Rayleigh-Jeans tail of the dust thermal emission, flux limited submillimeter surveys with 850 μm flux density $S_{850} > 5$ mJy reach an almost uniform integrated infrared (IR) luminosity limit across a wide redshift range ($1 < z < 8$) and yield a galaxy population mostly at redshifts between $1.7 < z < 2.8$ (Chapman et al. 2005). With star formation rates (SFRs) of $\sim 10^3$ $M_\odot$ yr^{-1}, the SMGs are the most intense star-forming galaxies, despite their inevitably short-lived nature (lifetime $\lesssim 0.1$ Gyr). Although such intense starburst systems are extremely rare in the local Universe, SMGs and the Lyman break galaxies may contribute equally to the comoving SFR density at $z \sim 4$ (Daddi et al. 2009). In addition to their unique energetics, they also represent an important stage in massive galaxy formation. Multiple lines of evidence suggest that SMGs are likely the progenitors of massive elliptical galaxies (e.g., Lilly et al. 1999; Swinbank et al. 2006; Aravena et al. 2010; Lapi et al. 2011; Hickox et al. 2012), which apparently have formed bulk of their stars rapidly at an early epoch (e.g., Renzini 2006).

Our understanding of this important high-redshift galaxy population are limited by the sensitivity and spatial resolution of current facilities. Gravitational lensing offers an elegant solution by effectively lifting both limiting factors. Also thanks to the negative K-correction, it is relatively straightforward to identify strongly lensed SMGs in large area submillimeter surveys. Blain (1996) and Negrello et al. (2007) predict that extragalactic sources with 500 μm flux density $S_{500} > 100$ mJy are mostly strongly lensed or blended SMGs, nearby late-type galaxies, and radio active galactic nuclei (AGNs). As demonstrated by Negrello et al. (2010), objects in the last two categories can be easily removed using data at other wavelengths, leading to an extremely high success rate in identifying strongly lensed SMGs with this technique (see also Vieira et al. 2010). This simple flux selection has produced a few well-studied strongly lensed SMGs (Lockman01 $z = 3.0$: Conley et al. 2011; Riechers et al. 2011a; Scott et al. 2011; ID141 $z = 4.2$: Cox et al. 2011; Bussmann et al. 2012; HLS J091828.6+514223 $z = 5.2$: Combes et al. 2012; and HATLAS12−00 $z = 3.3$, the subject of this paper), all of which were discovered by the *Herschel*[36] Space Observatory (Pilbratt et al. 2010). More complex selection processes have been proposed (e.g., González-Nuevo et al. 2012), which would allow selecting hundreds of fainter lensed galaxies with *Herschel*.

The brightest of the lensed SMGs might also be detected by the *Planck* mission (Planck Collaboration 2011a). With $\sim 4'$ resolutions, such sources are probably blended with fainter sources even in the highest frequency/resolution channels of *Planck* (545 and 857 GHz, or 550 and 350 μm). The Phase-I 130 deg^2 of the *Herschel*-Astrophysical Terahertz Large Area Survey (H-ATLAS; Eales et al. 2010) covers 28 *Planck* sources in the *Planck* Early Release Compact Source Catalog (ERCSC; Planck Collaboration 2011b). Herranz et al. (2012) find that sixteen of them are high Galactic latitude cirrus, ten are low-redshift galaxies, and one is resolved into two similarly bright nearby spirals

(NGC 3719 and 3720). Only one *Planck* source is dominated by high-redshift galaxies: PLCKERC857 G270.59+58.52 ($S_{550} = 1.4 \pm 0.6$ Jy, $S_{350} = 2.1 \pm 0.8$ Jy[37]). With 18″, 25″, and 36″ angular resolutions at 250, 350 and 500 μm, respectively, *Herschel* detect 16 objects within a 4.23′ radius of the *Planck* position (*Planck* has a full-width-half-maximum [FWHM] resolution of 4.23′ at 857 GHz). There are 15 faint ($S_{350} \sim 40$ mJy) sources surrounding an unusually bright source (HATLAS J114637.9−001132, hereafter HATLAS12−00; $S_{350} = 378 \pm 28$ mJy). Taking into account the differences in the beam size and the filter transmission, the *Herschel* sources account for only $\sim 28\%$ and $\sim 24\%$ of the *Planck* flux densities at 545 and 857 GHz, respectively, suggesting that the *Planck* measurements are boosted because of either positive noise spikes (i.e., "Eddington Bias"; Eddington 1913) or blending with an over-density of sources that are below the confusion limit of *Herschel* (Negrello et al. 2005). The reader is referred to Herranz et al. (2012) for a detailed *Planck-Herschel* comparison.

HATLAS12−00 peaks at 350 μm in flux density ("350 μm peaker"), implying a high photometric redshift given typical dust temperatures. Subsequent detections of multiple carbon-monoxide (CO) lines from this unusually bright object determined a redshift of $z_{CO} = 3.2592 \pm 0.0010$ (Zspectrometer, CARMA, Z-Spec; Harris et al. 2012, Van der Werf et al. in prep; Riechers et al. in prep). The high 500 μm flux density ($S_{500} = 298 \pm 24$ mJy), in combination with the confirmed high redshift, makes HATLAS12−00 an excellent strong lens candidate. It is also the only strongly lensed SMG candidate associated with a *Planck* detection in the entire 130 deg^2 H-ATLAS Phase-I region. Although the *Planck* detection is partly due to spurious factors (i.e., Eddington bias and/or blending), the confirmation of the lensed nature of the dominating source demonstrates that *Planck* can efficiently identify the brightest lensed SMGs once Galactic cirrus and low-redshift galaxies are removed.

In this paper we present a detailed multi-wavelength analysis of this *Planck*-associated SMG. We describe our high-resolution Keck adaptive optics imaging, Submillimeter Array (SMA) and Jansky Very Large Array (JVLA) interferometric observations, and the panchromatic photometry in § 2. We then perform a joint strong lens modeling at rest-frame 0.5 μm, 200 μm, and CO(1→0) in § 3. In § 4 we derive the intrinsic physical properties of the SMG from its spectral energy distribution (SED). We conclude by discussing the physical properties of HATLAS12−00 in the context of unlensed $z > 2$ SMGs (§ 5). Throughout we adopt a ΛCDM cosmology with $\Omega_m = 0.3$, $\Omega_\Lambda = 0.7$ and $H_0 = 70$ km s^{-1} Mpc^{-1}.

2. OBSERVATIONS

2.1. *Keck Adaptive Optics Imaging*

We obtained a 3,440-s K_S-band (hereafter K) image on 2011 April 13 (UT) and a 2,100-s J-band image on 2011 June 30 (UT) with the Keck II laser guide-star adaptive-optics system (LGSAO; Wizinowich et al. 2006). An $R = 15.8$ magnitude star 48″ SW of HATLAS12−00 served as the tip-tilt reference star. The estimated Strehl ratios at the source position are $\sim 23\%$ and 5% in K and J-band, respectively. We used the NIRC2 camera at 0″.04 pixel^{-1} scale for both filters (40″ field), and dithered with 2–3″ steps. The atmospheric see-

---
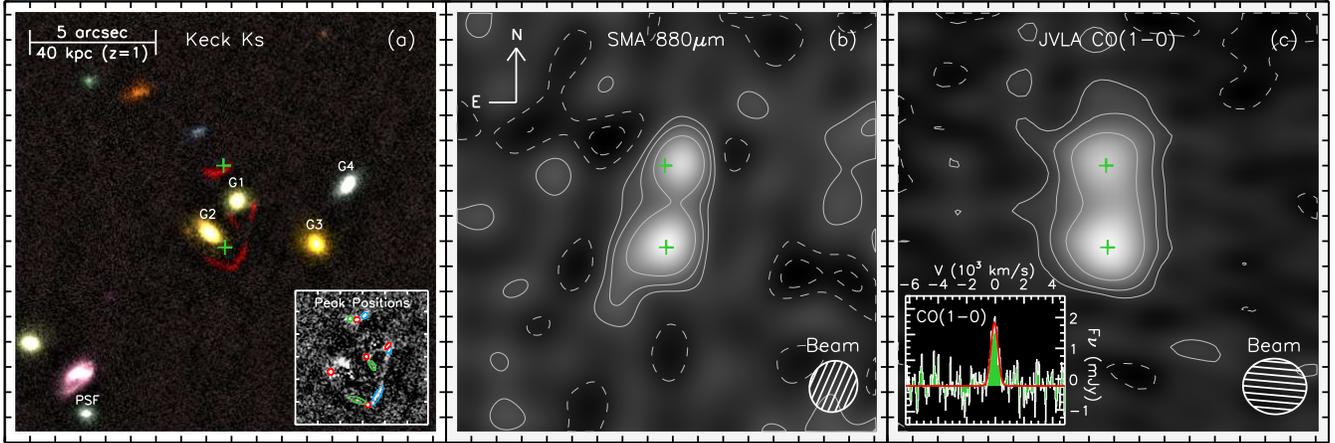
FIG. 1.— High-resolution images of HATLAS12−00. All images are aligned and the tickmarks are spaced at intervals of $1''$. Green crosses mark the two components seen in the JVLA image. *a*: Keck *K*-band image painted with a pseudo-colormap from Keck *K* (Red), *J* (Green), and ACAM optical (Blue) images. Lensing galaxies and the PSF star are labelled. The scale bar indicates $5''$ or 40 kpc at the lens redshift. The inset shows the lens-subtracted *K*-band image overlaid with the peak positions for lens modeling (§ 3.1). For clarity, the positional errors, as indicated by the ellipses, are enlarged by a factor of four. The colors distinguish images from the three clumps in the source plane. *b*: SMA 880 μm compact array image. Contours are drawn at $-2, -1, +1, +2$, and $+4\sigma$, where σ is the r.m.s. noise (3 mJy beam^{-1}). *c*: JVLA CO(1→0) image. Contours are drawn at $-1, +2, +4$, and $+8\sigma$, where σ is the r.m.s. noise (27 μJy beam^{-1}). The inset shows the CO spectrum from the same data cube, along with a Gaussian fit (red). In *b* and *c*, the ellipse to the lower right shows the beam.

ing at 0.5 μm was $\sim 0.4''$ and $0.5''$ during the *K* and *J*-band imaging, respectively[38].

We used our IDL (Interactive Data Language) programs to reduce the images. After dark subtraction and flat-fielding, sky background and object masks are updated iteratively. For each frame, after subtracting a scaled median sky, the residual background is removed with B-spline models. In the last iteration, we discard the three frames of the poorest image quality and correct the NIRC2 geometric distortion using the solution of P. B. Cameron[39] before combining the aligned frames. The resolution of the final *K* and *J*-band images are $0.''16$ and $0.''27$ in FWHM, respectively. We measure the FWHMs from the most compact source in the field located $10''$ SE of HATLAS12−00 (labeled "PSF" in Fig. 1*a*); we also use this object as the PSF in the lens modeling (§ 3.2). The images are flux calibrated against UKIRT Infrared Sky Survey (UKIDSS; Lawrence et al. 2007) and reach depths of $K = 25.6$ and $J = 25.0$ AB for a 5σ detection with $0.''1$ and $0.''2$ radius apertures[40], respectively.

2.2. *William Herschel Telescope Imaging*

Limited by the small field of NIRC2, a deep wide-field image is required for astrometry calibration. Optical imaging was obtained with the high-throughput auxiliary-port camera (ACAM) mounted at a folded-Cassegrain focus of the 4.2-m William Herschel Telescope (Benn et al. 2008) on 2011 April 26 (UT). We obtained four images of 200 s on a $\sim 2'$ field centered on HATLAS12−00, without any filter. The seeing was $\sim 0.''9$. The images were reduced and combined following standard techniques in IRAF[41]. No accurate photometric calibration is possible because we did not use any broad-band filter. But by comparing sources extracted from the ACAM image and the SDSS *i*-band catalog in the same field, we find that our image reaches an equivalent *i*-band 5-σ depth of 24.6 AB, or 2.3 magnitudes deeper than the SDSS.

We solve the astrometry of the ACAM image using the on-sky positions of Sloan Digital Sky Survey (SDSS; Aihara et al. 2011) DR8 sources inside the field. We use the astrometry routines in Marc Buie's IDL library[42] to correct for offsets, rotation, and distortions, with four terms (constant, X, Y, and $R = \sqrt{X^2 + Y^2}$). Sources that appear blended in the SDSS catalog are excluded. With 35 SDSS sources, we measure 1σ dispersions of δRA $= 0.''13$ and δDec $= 0.''14$ between the astrometry calibrated ACAM image and the SDSS. Finally, we use the same routines to match the NIRC2 images to the ACAM image with 13 well-detected sources inside the $40''$ NIRC2 field of view. The corrected NIRC2 images show 1σ dispersions of δRA $= 0.''04$ and δDec $= 0.''05$.

2.3. *SMA Submillimeter Imaging*

We obtained SMA interferometric imaging of HATLAS12−00 at 880 μm (339.58 GHz) in the compact array configuration with an on-source integration time ($t_{\rm int}$) of 1 hr and at 890 μm (336.9 GHz) in the subcompact array configuration with $t_{\rm int} = 2$ hr. The compact and subcompact observations took place on 2011 May 2 and 2012 January 14, respectively. During both nights, atmospheric opacity was low ($\tau_{225\,\rm GHz} \sim 0.1$) and phase stability was good. Both observations used an intermediate frequency coverage of 4–8 GHz and provide a total of 8 GHz bandwidth (considering both sidebands). The quasars 1229+020 and 1058+015 were used for time-variable gain (amplitude and phase) calibration. The blazar 3C 279 served as the primary bandpass calibrator. For the compact data, we used Titan as the absolute flux calibrator. For the subcompact data, we intended to use Callisto as the flux calibrator, but Jupiter might have fallen into one of the side lobes of the SMA primary beam while we observed Callisto. So we decided to use 3C 279 in lieu of Callisto as the flux calibrator. It is possible to use 3C 279 because we have reliable measurements of its flux both before and after the observation of HATLAS12−00.

We used the INVERT and CLEAN tasks in the Multi-channel Image Reconstruction, Image Analysis, and Display

---

[38] http://kiloaoloa.soest.hawaii.edu/current/seeing/

[39] http://www2.keck.hawaii.edu/inst/nirc2/forReDoc/post_observing/dewarp/

[40] Different aperture sizes were chosen here because of the different resolutions.

[41] http://iraf.noao.edu/

[42] http://www.boulder.swri.edu/~buie/idl/

(MIRIAD) software (Sault et al. 1995) to invert the *uv* visibilities and deconvolve the dirty map, respectively. We used natural weighting to obtain the best sensitivity. For the compact data, the CLEANed image has a synthesized beam with a FWHM resolution of $2\rlap{.}''07 \times 1\rlap{.}''87$ at a position angle (PA) of -23.6 degrees east of north; for the subcompact data, the beam is $5\rlap{.}''57 \times 3\rlap{.}''68$ at PA = 65.7 deg. The primary beam of the SMA is $\sim 37''$. The r.m.s. noise levels are 3.0 mJy beam^{-1} and 3.6 mJy beam^{-1} for the compact image and the subcompact image, respectively.

HATLAS12$-$00 is resolved into two components by the SMA (Fig. 1). Taking into account the 10% flux calibration uncertainty, the total flux is 70 ± 10 mJy and 93 ± 12 mJy for the compact image and the subcompact image, respectively. The latter agrees well with the LABOCA bolometer array flux measurement at 870 μm (§ 2.5). The compact array data did not fully capture the source flux because of the sparser array configuration, i.e., $\sim 25\%$ of the total flux is distributed on spatial scales larger than those accessible to the SMA in its compact array configuration. So we use the total flux from subcompact data for SED modeling (§ 4.2). We chose to use the compact image for lens modeling (§ 3.3) because of its higher spatial resolution. We find that using the subcompact image or the subcompact+compact combined image does not change the lens modeling result, but they give larger errors for the derived parameters.

2.4. *JVLA CO(1→0) Imaging*

We exploited the recent upgrade to the National Radio Astronomy Observatory[43]'s Very Large Array (Perley et al. 2011), which includes the provision of Ka-band receivers (26.5–40 GHz), to observe the redshifted CO(1→0) emission from HATLAS12$-$00 at 27.06532 GHz ($\nu_{\rm rest} = 115.27120$ GHz; Morton & Noreau 1994).

Observations were carried out dynamically during excellent weather conditions on 2012 January 6 and 8. During this Open Shared Risk Observing period the available bandwidth from the new Wideband Interferometric Digial ARchitecture (WIDAR) correlator consisted of two independently tunable output pairs of eight sub-bands each, with 64×2-MHz full-polarisation channels per sub-band, giving a total bandwidth of 2,048 MHz. At the redshift of HATLAS12$-$00, however, the CO(1→0) line could be reached by only the BD output pair, giving $\sim 11,350$ km s^{-1} coverage and ~ 22 km s^{-1} resolution. We offset our tuning by 64 MHz to avoid noisier edge channels. The 8 sub-bands of output pair AC were tuned to 32.5 GHz.

The bright compact calibration source, J1150$-$0023 were observed every few minutes to determine accurate complex gain solutions and bandpass corrections. 3C 286 ($S = 2.1666$ Jy at 27.06 GHz) was also observed to set the absolute flux scale, and the pointing accuracy was checked locally every hour. In total, around 2 hr of data were obtained for HATLAS12$-$00, with ~ 1 hr of calibration.

The data were reduced using $\mathcal{AIPS}$ (31DEC12) following the procedures described by Ivison et al. (2011), though with a number of important changes: data were loaded using BDF2AIPS and FRING was used to optimize the delays, based on 1 min of data for 3C 286. The base bands were knitted together using the NOIFS task, yielding *uv* datasets with

TABLE 1
PHOTOMETRY

Instrument	Band	λ (μm)	F_ν(G1+G2) (μJy)	F_ν(SMG) (mJy)
SDSS	u	0.36	0.1 ± 0.1	$\cdots$
	g	0.47	0.4 ± 0.4	$\cdots$
	r	0.62	3.3 ± 1.2	$\cdots$
	i	0.75	8.6 ± 2.0	$\cdots$
	z	0.89	23 ± 8	$\cdots$
UKIDSS	Y	1.03	35 ± 6	$\cdots$
	J	1.25	67 ± 8	0.0017 ± 0.0003
	H	1.63	68 ± 10	$\cdots$
	K	2.20	139 ± 10	0.0123 ± 0.0009
WISE	$w1$	3.35	205 ± 20	0.037 ± 0.020
	$w2$	4.60	242 ± 53	$\lesssim 0.117$
	$w3$	11.56	735 ± 35	$\lesssim 0.702$
	$w4$	22.09	< 3460	$\cdots$
PACS	green	100	$\cdots$	25 ± 6
	red	160	$\cdots$	138 ± 21
SPIRE	blue	250	$\cdots$	323 ± 24
	green	350	$\cdots$	378 ± 28
	red	500	$\cdots$	298 ± 24
LABOCA	$\cdots$	870	$\cdots$	103 ± 19
SMA	$\cdots$	890	$\cdots$	93 ± 12
MAMBO	$\cdots$	1200	$\cdots$	38 ± 6
CARMA	$\cdots$	2792	$\cdots$	1.4 ± 0.5
	$\cdots$	3722	$\cdots$	< 2.0
VLA	$\cdots$	214000	$\cdots$	1.2 ± 0.4

512×2-MHz channels, which we then added together using the task DBCON. Finally, the channels were imaged over a $512 \times 512 \times 0.3''$ field, with natural weighting (ROBUST = 5), to form a 512^3 cube centered on HATLAS12$-$00. Integrating over those 55 channels found to contain line emission (so a FWZI of $\sim 1,200$ km s^{-1}) yielded an r.m.s. noise level of 27 μJy beam^{-1}.

The CLEANed and velocity-integrated CO map is shown in Fig. 1c. The beam is $2\rlap{.}''5 \times 2\rlap{.}''2$ at PA = 85°. Similar to the SMA, the map resolves two components separated by $\sim 5''$. The CO lines extracted from the two components show the same redshift and line profile, further confirming that they are lensed images of a single source. The best-fit Gaussian to the area-integrated spectrum gives a line width of $\Delta V_{\rm FWHM} = 585 \pm 55$ km s^{-1} and a line flux of $S_{\rm CO}\Delta V = 1.52 \pm 0.20$ Jy km s^{-1}. In comparison, the CO(1→0) measurements reported by Harris et al. (2012) using Zpectrometer on the Green Bank Telescope are: $\Delta V_{\rm FWHM} = 680 \pm 80$ km s^{-1} and $S_{\rm CO}\Delta V = 1.18 \pm 0.26$ Jy km s^{-1} (corrected for the 20% difference in the absolute flux density of 3C 286). The reason for the discrepancy is unclear, but the two line flux measurements agree within the 1σ errors. So hereafter, we use the weighted mean of the two measurements, $S_{\rm CO}\Delta V = 1.40 \pm 0.22$ Jy km s^{-1}, to derive the molecular gas mass.

2.5. *Panchromatic Photometry*

Photometry of HATLAS12$-$00 were obtained from the SDSS ($u, g, r, i,$ and z), the UKIDSS ($Y, J, H,$ and K), the Wide-Field Infrared Survey Explorer (*WISE*, 3.6 and 4.6 μm; Wright et al. 2010), the *Herschel*/PACS (100 and 160 μm; Program ID: OT1_RIVISON_1; Ibar et al. 2010), the *Herschel*/SPIRE (250, 350, and 500 μm; Pascale et al. 2011; Rigby et al. 2011), the Large APEX BOlometer CAmera (LABOCA, 870 μm; Siringo et al. 2009), the SMA (880 μm), the Max-Planck Millimetre Bolometer (MAMBO, 1.2 mm; Kreysa et al. 1999), the Combined Array for Research in

Millimeter-wave Astronomy (CARMA, 2792 and 3722 μm; Bock et al. 2006), and the VLA FIRST survey (21 cm; Becker et al. 1995).

We obtained imaging at 870 μm with the LABOCA bolometer array at the Atacama Pathfinder EXperiment (APEX) telescope in November 2011 (Clements et al. in prep). LABOCA observed a 11.4′ diameter field with a resolution of FWHM = 18.″6. The observations have a total integration time of ∼30 hr reaching a 1σ sensitivity of ∼2 mJy.

We obtained 1.2 mm imaging with MAMBO at the IRAM 30-m telescope (FWHM ∼ 10.″7) in January and February 2011 (Dannerbauer et al. in prep.). Observing time in the on-off mode is 24 minutes, achieving a 1σ sensitivity of ∼1 mJy.

We obtained continuum observations at 81.2 and 108.2 GHz (3722 and 2792 μm; covering rest-frame CO[3→2] and CO[4→3] lines) on 2011 Mar 18 and Sep 1 as part of our CO follow-up campaign of bright, lensed H-ATLAS SMGs with CARMA in D array (Riechers et al. in prep). Observations were carried out for 0.9 and 1.4 hr on source, respectively, using the 3 mm receivers and a bandwidth of 3.7 GHz per sideband. HATLAS12−00 is unresolved in these observations, with angular resolutions of $6.″8 \times 5.″0$ and $6.″0 \times 3.″8$ at 81.2 and 108.2 GHz, respectively (restored with natural baseline weighting).

Table 1 lists the photometry. We have included in the errors the absolute flux calibration uncertainties (3% for *WISE*, 3−5% for PACS, 7% for SPIRE, 10% for SMA, and 15% for LABOCA, MAMBO, and CARMA).

3. LENS MODELING

Because the LGSAO image has the highest spatial resolution, we use it to find the best-fit lens model. We initially use the peak positions of the multiply-imaged source to constrain the lensing potentials (§ 3.1), then we exploit the *K*-band light distribution in the image plane to quantify the morphologies of the source as well as refining the lensing potentials (§ 3.2). Finally, we use the best-fit lensing potentials and the SMA and JVLA images to constrain the sizes and locations of the dust and molecular gas in the source plane (§ 3.3 & 3.4).

3.1. *K-band Peak Positions*

We use LENSTOOL (Kneib et al. 1996; Jullo et al. 2007) to find the best-fit parameters and their errors from the peak positions. LENSTOOL implements a Bayesian Markov chain Monte-Carlo sampler to derive the posterior distribution of each parameter and an estimate of the evidence for the model.

The lensing system is mainly made of two red filaments that are ∼3.″5 apart (Fig. 1*a*). The outward curved shape of the northern arc can be explained if the source is intrinsically curved. Hence we split each of the two arcs into three parts and build a simple lens model by putting two deflectors centered on G1 and G2. We find that the predicted counter-images can explain the additional features close to G1 and G2. Guided by the predicted counter-images, we define three systems of lensed images (Fig. 1*a* inset). The 11 peak positions in 3 separate systems provide a total of 16 constraints $(11 \times 2 - 3 \times 2)$, allowing us to include shear from nearby galaxies G3 and G4.

For the lensing galaxies, we find photometric redshifts of $z_{G1+G2} = 1.06 \pm 0.16$ and $z_{G4} = 0.80 \pm 0.28$ with the public photo-*z* code EAZY (Brammer et al. 2008). We obtain the nine-band photometry from the SDSS (u, g, r, i, and z) and the UKIDSS (Y, J, H, and K) surveys. At these wavelengths, the flux from the lensed galaxy is negligible (§ 4). The redshift of G1+G2 is measured from the total fluxes of G1 and G2, because they are blended in the seeing limited data. G3 is undetected in SDSS but shows similar color as G1 and G2. Hence in the lens modeling we assume all four galaxies are at $z = 1.06$. Note that although redshift errors of the lensing galaxies would lead to errors in the estimated lens masses, they would not change our conclusions on the lensed galaxy because the magnification factors would remain the same.

For the lens model, we assume that the dark-matter plus baryonic mass profiles of the foreground lens galaxies G1 to G4 can be described as singular isothermal ellipsoids (SIEs; Kormann et al. 1994). The SIE profile is parametrized by the velocity dispersion (σ), the position (x, y), the axis ratio ($q = b/a$), and the PA (θ, E of N). We fix the positions to the centers of the galaxies. For G3 and G4, we further fix their q and θ to those from the light distribution, because they are not well constrained by the peak positions and there are significant correlations between the PA and ellipticity of the light and of the mass distribution (e.g. Sluse et al. 2011). Therefore, we have a total of eight free parameters. We find a best-fit with $\chi^2 = 7.9$ for dof = 8 (degrees of freedom) and an average positional error of 0.″04 (∼1 pixel). The parameters and their errors are summarized in Table 2. We also list the mass enclosed by the critical curve for each SIE,

$$M_E = \frac{4\pi^2}{G} \frac{D_L D_{LS}}{D_S} \frac{\sigma^4}{c^2}, \quad (1)$$

where D_L, D_S, and D_{LS} are the angular diameter distances to the lens, to the source, and between the lens and the source, respectively. The radius of the area enclosed by the critical curve can be approximated by the circularized Einstein radius:

$$b = 4.5 (\frac{\sigma}{200 \text{ km s}^{-1}})^2 \sqrt{\frac{2q}{1+q^2}} \text{ kpc}. \quad (2)$$

In the errors of masses and velocity dispersions, we have included the 1-σ uncertainty of the photometric redshift.

The nominal model described above is the most favorable description of the lensing system because of the following:

1. Adding q's and θ's of G3 and G4 as free parameters does not substantially improve the fit: the Bayesian evidence[44] increases by only $\Delta \ln(E) = 0.5$ and the reduced χ^2 actually increases from 1.0 to 1.6 as a result of the decreased degree of freedom.

2. Excluding the potentials of G3 and/or G4 does degrade the fit significantly. The Bayesian evidence decreases by $\Delta \ln(E) = 2.5$ and 30, and the reduced χ^2 increases from 1.0 to 1.8 and 6.5, when we exclude G4 and both G3 and G4, respectively.

3. Including a group-scale potential with a PIEMD profile (Pseudo-Isothermal Elliptic Mass Distribution; Kassiola & Kovner 1993) does not improve the fit. For the PIEMD profile, we adopt a cut-off radius of 500 kpc but allow the position, ellipticity, PA, core radius, and velocity dispersion to vary. To limit the number of free parameters, we fix the q's and PA's of the SIEs to those

---

[44] The improvement of a model is substantial if $1 < \Delta \ln(E) < 2.5$, strong if $2.5 < \Delta \ln(E) < 5$, and decisive if $\Delta \ln(E) > 5$ (Jeffreys 1961).

TABLE 2
DERIVED PROPERTIES FROM LENS MODELING

Object	Quantity	Value		Unit
		Peak Position[a]	Surface Brightness[b]	
G1	q	0.46 ± 0.10	0.52 ± 0.04	$\cdots$
$\cdots$	θ	-59 ± 10	-61 ± 2	deg
$\cdots$	σ	209 ± 24	212 ± 24	km s^{-1}
$\cdots$	M^c	$1.6^{+0.9}_{-0.6} \times 10^{11}$	$1.7^{+0.9}_{-0.7} \times 10^{11}$	M$_\odot$
G2	q	0.63 ± 0.06	0.69 ± 0.03	$\cdots$
$\cdots$	θ	59 ± 7	67 ± 2	deg
$\cdots$	σ	240 ± 28	240 ± 27	km s^{-1}
$\cdots$	M^c	$2.7^{+1.5}_{-1.1} \times 10^{11}$	$2.7^{+1.5}_{-1.1} \times 10^{11}$	M$_\odot$
G3	σ	243 ± 51	242 ± 28	km s^{-1}
$\cdots$	M^c	$2.9^{+3.3}_{-1.8} \times 10^{11}$	$2.8^{+1.5}_{-1.1} \times 10^{11}$	M$_\odot$
G4	σ	168 ± 40	165 ± 20	km s^{-1}
$\cdots$	M^c	$6.6^{+8.9}_{-4.4} \times 10^{10}$	$6.1^{+3.6}_{-2.4} \times 10^{10}$	M$_\odot$
SMG	$\mu(K)$	$\cdots$	16.7 ± 0.8	$\cdots$
$\cdots$	$\mu(880\mu m)$	$\cdots$	7.6 ± 1.5	$\cdots$
$\cdots$	$\mu(CO)$	$\cdots$	6.9 ± 1.6	$\cdots$

NOTE. — a - Best-fit parameters from the K-band peak positions (§ 3.1). b - Best-fit parameters from the K-band surface brightness distribution (§ 3.2). c - Total mass enclosed by the critical curve of each SIE potential (Eqs. 1 & 2).

measured from the lensing galaxies but allow their velocity dispersions to vary. So we have a total of 10 free parameters. The reduced χ^2 of the best-fit is 1.9, much higher than that of the nominal model. The Bayesian evidence also decreases by $\Delta \ln(E) = 6.9$ when compared with the nominal model.

3.2. K-band Source

Although the peak positions can constrain the deflectors through ray tracing, they cannot provide an accurate estimate of the magnification factor because the source-plane light distribution is not taken into account. Because we want to estimate the intrinsic properties of the lensed galaxy, we are interested in the luminosity weighted magnification factor, which depends on the source morphology because the magnification factor is different at each source plane position. In this section we model the morphology of the lensed galaxy and refining the lensing potentials simultaneously with the K-band image. The PSF is derived from the most compact source in the field, which is $10''$ SE of HATLAS12−00 (Fig. 1a).

Following § 3.1, we assume that the source consists of three clumps, each described as a Sérsic profile. Again we use SIE profiles for the lensing potentials. So we have a total of 29 parameters: seven parameters for each Sérsic profile, and eight parameters for the SIE potentials. Our fitting procedure is as follows. For an initial set of parameters describing the source and the lenses from § 3.1, we use LENSTOOL to generate lensed images of the source, which is then convolved with the PSF and compared with the observed image. We limit the comparison in a $3''.3 \times 4''.5$ (83×113 pixels) rectangular region that encloses the lensing features. This process is iterated with AMOEBA_SA to find the parameters that minimize the residual between the observation and the model. AMOEBA_SA is based on the IDL multidimensional minimization routine AMOEBA (Press et al. 1992) with simulated annealing added by E. Rosolowsky. We allow a maximum of 1000 iterations in each call of AMOEBA_SA. For the simulated annealing, we adopt an initial "temperature" of 100 and

decrease it by 20% in each subsequent call to AMOEBA_SA. A good fit with a reduced χ^2 around unity is normally found after a few calls to AMOEBA_SA. For each iteration, we compute the total luminosity-weighted magnification factor (μ_K) by summing the pixel values in the image and the source planes with apertures matched by inverting the image plane aperture to the source plane. The 1-σ confidence interval of μ_K is found with $\chi^2(\mu) - \chi^2_{\min} \leq 1$. Note that we compute the χ^2 values on the residual image binned by 4-pixel boxes (FWHM = $0''.16$ = 4 pixel), so that the noise becomes uncorrelated between pixels; or equivalently, one could divide the χ^2 values from the original residual images by a factor of 16. We find the luminosity-weighted magnification to be $\mu_K = 16.7 \pm 0.8$. The best-fit parameters for the deflectors are listed in Table 2. The results are very similar to those from fitting the peak positions, although the errors are smaller because the entire image provides more information than the peak positions alone.

Figure 2 shows the best-fit model. The lensed galaxy has a curved morphology, causing the northern arc bending in the opposite direction of the deflectors. In the source plane, the three clumps extend over only $0''.21$ or 1.6 kpc, and their effective radii are $0''.21 \pm 0''.04$ (1.5 ± 0.3 kpc), $0''.085 \pm 0''.013$ (0.6 ± 0.1 kpc), and $0''.11 \pm 0''.05$ (0.8 ± 0.4 kpc) from W to E.

The nature of the feature NNE of G2 in the residual image is unclear, but it is unlikely to be at the same redshift as the lensed galaxy: tracing its position to the source plane and imaging it back predicts an *unobserved* equally bright counter-image $0''.8$ S of the southern arc. This feature could therefore be part of the galaxy G2.

3.3. 880 μm Source

Precise astrometry calibration is crucial for a joint analysis of images from different wavelengths. Because the only K source detected by the SMA is HATLAS12−00, we have to estimate the astrometry offset between the two images in a statistical way. Because the Keck image is tied to the SDSS astrometry and the SMA image is tied to the radio reference frame, we cross-correlate the VLA FIRST catalog (Becker et al. 1995) and the SDSS catalog within $1°$ of HATLAS12−00 and compute the optical-radio separation. Ninety-four radio sources have optical counterparts within $3''$. We then fit an elliptical Gaussian to the two-dimensional distribution in $\Delta RA = -(\alpha_{FIRST} - \alpha_{SDSS})$ and $\Delta Dec = \delta_{FIRST} - \delta_{SDSS}$. The systematic offset from the peak position of the Gaussian is consistent with zero ($\Delta RA = -0''.07$, $\Delta Dec = +0''.08$). The best-fit Gaussian has σ's of $0''.40$ and $0''.30$, and a PA of $119°$ for the major axis. Therefore, the 1σ ellipse of the astrometry offset has major/minor semi-axes of $0''.61/0''.45$. Our result is consistent with that of Ivezić et al. (2002), who found a $\sim 0''.1$ systematic offset and a 1σ error circle of $0''.47$ in radius between FIRST and SDSS astrometry.

We can constrain the astrometry offset further through lens modeling. As demonstrated by Kochanek & Narayan (1992) and Wucknitz (2004), interferometric data are most naturally modeled with the uv-plane visibilities, because it avoids beam deconvolution and naturally handles correlated noise. Here, however, we opt to model the CLEANed map directly, because (1) the images are essentially unresolved in the SMA map, and (2) we already have a good lens model from the K-band image (§ 3.2). Because of the limited spatial resolution of the
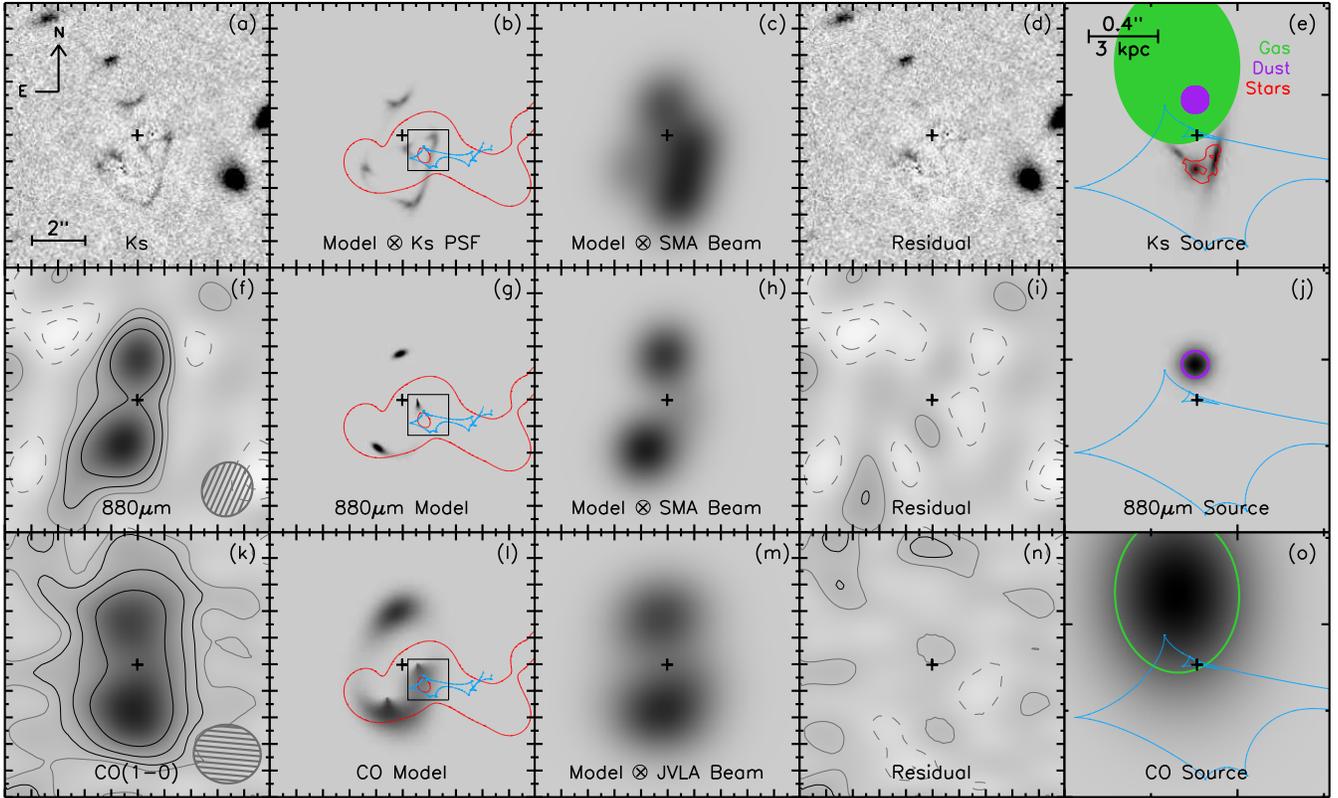
FIG. 2.— Lens modeling results. Major tickmarks are spaced at intervals of $1''$. To ease comparisons, a cross is drawn at the center of each panel. *a*: Keck K image after subtracting G1 and G2. *b*: Best-fit K model convolved with the K-band PSF. Critical curves are in red and caustics are in blue. The box delineates the region covered by the source images (i.e., *e*, *j*, and *o*). *c*: K model convolved with the SMA beam. It is clearly different from the SMA and JVLA images (*f* & *k*), indicating differential magnification. *d*: K residual. *e*: Modeled intrinsic source morphology (i.e., without PSF; grey scale) vs. a direct inversion of the observed image (red contours). For comparison, the 880 μm (*purple*) and CO(1→0) (*green*) sources are shown as color-filled ellipses. *f*: SMA 880 μm compact array image. The grey ellipse shows the beam. Here and in *i*, contours are drawn at $-2, -1, +1, +2,$ and $+4\sigma$, where σ is the r.m.s. noise (3 mJy beam^{-1}). *g*: 880 μm model. *h*: Model convolved with the SMA beam. *i*: 880 μm residual. *j*: 880 μm source. The purple circle shows the FWHM of the source. *k*: JVLA CO(1→0) image. Here and in *n*, contours are drawn at $-1, +1, +2, +4,$ and $+8\sigma$, where σ is the r.m.s. noise (27 μJy beam^{-1}). *l*: CO model. *m*: Model convolved with the JVLA beam. *n*: CO residual. *o*: CO source. The green ellipse shows the FWHMs of the source.

SMA 880 μm image, the two centroid positions do not offer enough information to constrain the lens model. Hence, for the deflectors, we fix all the parameters to the best-fit values from § 3.2; for the source, we assume a circular Gaussian profile with variable position and size. We shift the SMA image relative to the K model on a $2'' \times 2''$ grid with $0''.1$ steps. At each offset position, we find the best-fit model using the same fitting procedure as in § 3.2. The modeling is performed on a 51×68-pixel ($5''.1 \times 6''.8$) region enclosing the SMA sources. Figure 3a shows a map of the minimum χ^2 values at each offset position. The global best-fit, with reduced χ^2 of unity, is reached when we shift the SMA image $0''.6$ E of the K image. The middle panels of Fig. 2 show this global best-fit model.

The noise of the SMA map is Gaussian but is highly correlated. We compute the r.m.s. noise of the SMA map after binning it by boxes of n^2 pixels. We find that the noise starts to decrease as $1/n$ for $n \gtrsim 20$ pixels (FWHM $\simeq 2'' = 20$ pixel), indicating that the noise becomes uncorrelated on 20-pixel scales. Therefore, we divide the χ^2 values from the the residual images by a factor of 400, which is equivalent to computing χ^2 from residual images binned by 20-pixel boxes.

In combination with the 1σ error ellipse from FIRST–SDSS cross-correlation, we determine that the astrometry offset between 880 μm and K images is ΔRA $= -0''.5 \pm 0''.1$ and ΔDec $= 0''.0 \pm 0''.2$; i.e., the overlapping region between

the ellipse and the 1σ contour of the χ^2 map. Collecting all of the solutions in this permitted offset region satisfying $\chi^2(\mu) - \chi^2_{\min} \leq 1$, we estimate a luminosity-weighted 880 μm magnification of $\mu_{880} = 7.6 \pm 1.5$, and an 880 μm source size of FWHM $= 0''.15^{+0.14}_{-0.06} = 1.2^{+1.0}_{-0.5}$ kpc. Because we have fixed the deflectors with the best-fit parameters from K-band, the errors here do not include the uncertainties of the deflectors. Higher resolution far-IR images are required to constrain the deflectors and the source simultaneously.

Dust emitting regions are often spatially offset from the UV/optical emitting regions in SMGs (Tacconi et al. 2008; Bothwell et al. 2010; Carilli et al. 2010; Ivison et al. 2010b; Riechers et al. 2010). This is clearly the case for HATLAS12−00, which shows distinctly different morphologies at K-band and 880 μm, even after convolving the K-band image with the SMA beam (compare Fig. 2c & f). From the lens model, we estimate a source-plane separation between the 880 μm source and the central K clump of $0''.41 \pm 0''.07$ or 3.1 ± 0.5 kpc (Fig. 2e).

If we assume zero astrometry offset between SMA and Keck, then we obtain a model that poorly fits the observation ($\Delta \chi^2 \sim 4$; Fig. 3a). The lens model gives a slightly larger magnification ($\mu_{880} = 8.4 \pm 1.6$) and doubles the source size (FWHM $= 2.5^{+1.9}_{-0.3}$ kpc). However, the source-plane separation between the 880 μm source and the central K clump remains the same (3.2 ± 0.2 kpc).
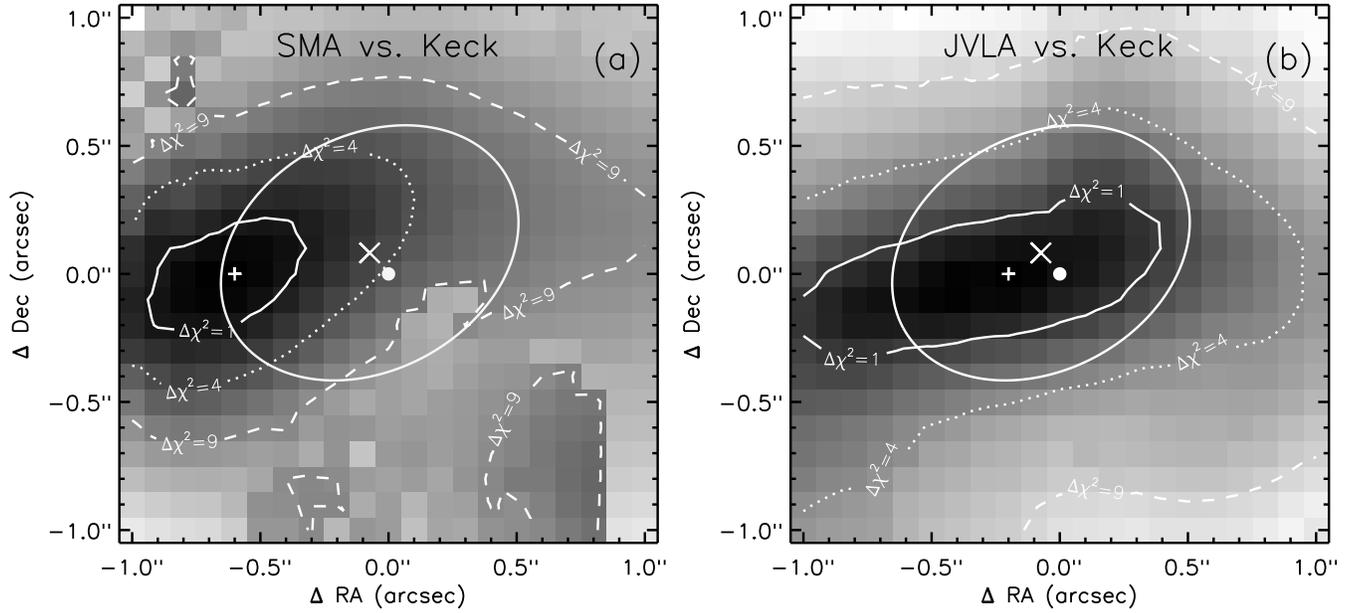
FIG. 3.— Constraining the astrometric offset between SMA, JVLA and Keck. *a*: The background image is the χ^2 map of the best-fit models as a function of SMA−Keck offset. The image is displayed in logarithmic scale. Positive offsets indicate shifting the SMA image W or N relative to the Keck image. Iso-χ^2 contours are overlaid for 1, 2, and 3σ intervals. The white plus sign indicates the offset that yields the minimum χ^2 value. The ellipse shows the 1σ astrometry uncertainty determined from FIRST–SDSS cross-correlation. The cross indicates the systematic offset ($-0.''07$, $+0.''08$) between FIRST and SDSS within 1° radius of HATLAS12−00. The overlapping area between the 1σ contour of the χ^2 map and the ellipse gives the best estimate of the astrometric offset and its uncertainty. Zero offset is indicated by the white circle. *b*: Same as *a* but for JVLA relative to Keck.

3.4. *CO(1→0) Source*

We use the same technique to model the JVLA CO(1→0) map as in § 3.3. The lensed images are better resolved in the JVLA image than in the SMA image, so we use an elliptical Gaussian instead of a circular Gaussian for the source profile. The model has a total of six free parameters (x, y, FWHM, q, PA, and flux density). Again, we can constrain the astrometric offset between JVLA and Keck through lens modeling. Figure 3*b* shows the minimum χ^2 values at each offset position relative to the *K* image. To deal with the correlated noise, we scale the χ^2 values from the residual map by the product of the FWHMs of the major and minor axes of the beam. The global best-fit, with reduced χ^2 of unity, is reached when we shift the JVLA image $0.''2$ E of the *K* image. The bottom panels of Fig. 2 show the best-fit model. We estimate a CO magnification of $\mu_{CO} = 6.9 \pm 1.6$. Similar to the SMA image, we find a source-plane separation of 4.7 ± 1.6 kpc between the cold molecular gas and the stellar emission (i.e., the central *K* clump). The CO(1→0) is emitted from a more extended region than the dust, but the two spatially overlap (Fig. 2*e*). The CO source has FWHM = $0.''9 \pm 0.''3 = 6.8 \pm 2.3$ kpc along the major axis, with an axis ratio of $0.8^{+0.2}_{-0.6}$.

The molecular gas disk is massive. The velocity-area-integrated CO brightness temperature of $L'_{CO} = [6.4 \pm 1.0] \times 10^{11}$ K km s^{-1} pc^2 indicates a molecular gas reservoir of $M_{gas} = [7.4 \pm 2.1] \times 10^{10}$ M$_\odot$ after lensing correction, assuming a conversion factor of $\alpha_{CO} = M_{gas}/L'_{CO} = 0.8$ M$_\odot$ (K km s^{-1} pc^2)$^{-1}$, which is commonly assumed for starburst environments (Solomon & Vanden Bout 2005). Note, however, that α_{CO} is uncertain by at least a factor of a few and it may depend on the metallicity, the gas temperature, and the velocity dispersion of the galaxy (Narayanan et al. 2012).

The CO magnification factor determined from the lens model (6.9 ± 1.6) is in excellent agreement with that estimated from the CO luminosity−FWHM correlation. The observed L'_{CO} and line width indicates a magnification factor of 7 ± 2, based on its deviation from the correlation established by un-lensed SMGs (Harris et al. 2012, Bothwell et al. in prep). This agreement demonstrates that strongly lensed SMGs may be effectively selected with CO spectroscopy in the future.

4. SPECTRAL ENERGY DISTRIBUTIONS

Useful physical parameters are encoded in the SEDs. The optical-to-NIR SED of HATLAS12−00 is dominated by the foreground galaxies G1 and G2, from which we can derive the photometric redshift and the stellar population of the lensing galaxies. The far-IR and submillimeter regime is dominated by the lensed SMG, as evident in the SMA image, so the data can tell us the dust and star formation properties of the SMG.

4.1. *Lensing Galaxies*

Adopting the photometric redshift of 1.06, we model the nine-band photometry (*u*, *g*, *r*, *i*, *z*, *Y*, *J*, *H*, and *K*) of G1+G2 with the stellar population synthesis models of Bruzual & Charlot (2003, BC03). We assume a Chabrier (2003) initial mass function (IMF), Calzetti et al. (1994) extinction law, and exponentially declining star formation history, with a range of e-folding times ($\tau = 0.1$ to 30 Gyr) and ages (0.01 to 12.5 Gyr). For each template, we fit for the stellar mass ($M_{stellar}$) and extinction ($E(B-V)$). The best-fit model gives $\chi^2 = 6.4$ for dof = 7 (Fig. 4*a*). The derived properties of G1+G2 are listed in Table 3. The intrinsic extinction is small ($E(B-V) = 0.04^{+0.11}_{-0.04}$) and there is very little current star formation (SFR = $0.1^{+0.4}_{-0.1}$ M$_\odot$ yr^{-1}). The dust-absorbed UV/optical luminosity ($[3^{+14}_{-3}] \times 10^{10}$ L$_\odot$) is less than 0.15%
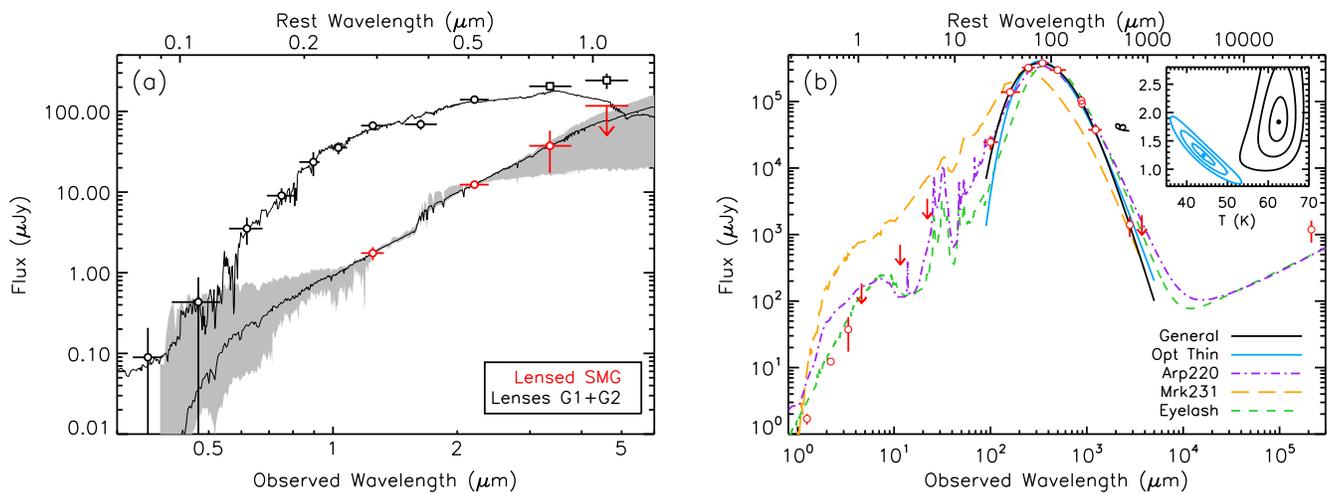
FIG. 4.— Modeling the SEDs. Top axes indicate wavelengths at the rest frame of the SMG ($z = 3.26$). *a*: Black data points are for the foreground lenses G1+G2, and the red data points are for the lensed SMG. The top black curve shows the best-fit BC03 stellar population synthesis model of G1+G2 at $z = 1.06$, using the nine data points below 3 μm. The bottom black curve shows the best-fit BC03 model for the SMG, along with the 1σ range of acceptable models. *b*: The full SED of the SMG. The short dashed (*green*), dash-doted (*purple*), and long dashed (*orange*) curves are the best-fit SED templates of the "Cosmic Eyelash" (Ivison et al. 2010c), Arp 220, and Mrk 231, respectively. The Eyelash provides the best description of the overall SED among the three. The solid black and blue curves are the best-fit models with a single-temperature modified blackbody using the general and optically thin formula, respectively. The inset shows the 1, 2, and 3σ contours in the $T - \beta$ plane for the general (*black*) and optically thin (*blue*) models.

TABLE 3
DERIVED PHYSICAL PROPERTIES

Object	Quantity	Value	Unit
G1+G2	$M_{\rm stellar}$	$3.5^{+1.8}_{-1.1} \times 10^{11}$	$M_\odot$
$\cdots$	Age	3 ± 2	Gyr
$\cdots$	τ	0.3 ± 0.2	Gyr
$\cdots$	$E(B-V)$	$0.04^{+0.11}_{-0.04}$	mag
$\cdots$	$SFR_{\rm opt}$	$0.1^{+0.4}_{-0.1}$	$M_\odot$ yr^{-1}
SMG[a]	$M_{\rm stellar}$	$[3.5 \pm 2.4] \times 10^{10}$	$M_\odot$
$\cdots$	$SFR_{\rm opt}$	1000 ± 1000	$M_\odot$ yr^{-1}
SMG[b]	$T_{\rm dust}$	63 ± 2	K
$\cdots$	β	1.8 ± 0.4	$\cdots$
$\cdots$	$M_{\rm dust}$	$[7.0 \pm 2.0] \times 10^{8}$	$M_\odot$
$\cdots$	λ_0	250 ± 40	μm
$\cdots$	σ	0.8 ± 0.2	kpc^2
$\cdots$	$L_{\rm IR}$	$[1.7 \pm 0.3] \times 10^{13}$	$L_\odot$
$\cdots$	$SFR_{\rm IR}$	1900 ± 400	$M_\odot$ yr^{-1}
SMG[c]	$T_{\rm dust}$	44 ± 3	K
$\cdots$	β	1.3 ± 0.2	$\cdots$
$\cdots$	$M_{\rm dust}$	$[1.0 \pm 0.3] \times 10^{9}$	$M_\odot$
SMG[d]	$L'_{\rm CO}$	$[9.3 \pm 2.6] \times 10^{10}$	K km s^{-1} pc^2
$\cdots$	$L_{\rm IR}/L'_{\rm CO}$	172 ± 58	$L_\odot$/K km s^{-1} pc^2
$\cdots$	FWHM$_{\rm CO}$	585 ± 55	km s^{-1}
$\cdots$	$M_{\rm gas}$	$[7.4 \pm 2.1] \times 10^{10}$	$M_\odot$
$\cdots$	$M_{\rm dyn}$	$[3.2 \pm 1.3] \times 10^{11}$	$M_\odot$
$\cdots$	$M_{\rm gas}/M_{\rm baryon}$	$68 \pm 17\%$	$\cdots$
$\cdots$	$M_{\rm gas}/M_{\rm dyn}$	$23 \pm 11\%$	$\cdots$

NOTE. — Magnification-dependent parameters have been de-magnified and their errors include the magnification uncertainties. *a* - Stellar population synthesis modeling of the near-IR SED. *b* - General "optically thick" modified blackbody fit to the far-IR-to-mm SED. *c* - Optically thin modified blackbody fit. *d* - Parameters derived from CO(1→0) observations.

of the total integrated IR luminosity before lensing correction ($L_{8-1000} = 1.2 \times 10^{14}$ L$_\odot$). Therefore, G1 and G2 do not contribute significantly to the far-IR fluxes, in agreement with their absence in the SMA image. The stellar mass from SED modeling is $\sim$80% of the total mass within the critical curves from lens modeling (Table 3), implying that the galaxies are dominated by stellar mass within ~ 7 kpc.

4.2. *Lensed SMG*

In the *J* and *K*-bands, we obtain the photometry of the SMG with an aperture contoured around the multiply-imaged features after subtracting the foreground lenses. We measure $K = 21.2 \pm 0.1$ and $(J - K) = 2.1 \pm 0.2$ in AB magnitudes, consistent with the red $J - K$ colors of unlensed SMGs (Frayer et al. 2004; Dannerbauer et al. 2004). Careful modeling is required to extract SMG photometry from the *WISE* data, because the SMG is blended with the foreground galaxies G1 through G4 (FWHM = 6–12″). We model the *WISE* 3.4 μm source with four elliptical Gaussians of the same shape. With GALFIT (Peng et al. 2010), we fix their positions to those determined from the Keck image, but we allow the Gaussian shape to vary. Then we measure the flux density of G1+G2 ($\sim$205 μJy) decomposed from that of G3 and G4 ($\sim$117 μJy). Finally, the flux density of the SMG ($\sim$37 μJy) is estimated from the excess of G1+G2 relative to their best-fit stellar population synthesis model (§ 4.1). Unfortunately, we can not separate G3+G4 from G1+G2 in the longer wavelength channels of *WISE* because of the inferior image quality, so we treat the excesses over the best-fit model of G1+G2 as upper limits for the SMG. The far-IR-to-millimeter SED is dominated by the lensed SMG, therefore no foreground subtraction is necessary. Table 1 summarizes the photometry for HATLAS12−00.

We opt to model the rest-frame optical and far-IR emission separately, instead of fitting them together in a self-consistent way with MAGPHYS (da Cunha et al. 2008), because our lens model shows that they are emitted from physically distinctive regions, i.e., the dust that attenuates the optical emission has little to do with the starburst-heated dust that emits in the far-IR.

It is difficult to constrain the stellar population with only three photometric detections (dof = 1) in rest-frame optical.

However, we can limit the parameter space by excluding unphysical models, such as those that require negative extinction corrections and those whose ages exceed the cosmic age at $z = 3.2592$ (1.9 Gyr). We use the same BC03 templates as in the previous section. The shaded region in Fig. 4a shows all of the permitted models with $\chi^2 < \mathrm{dof} + 1$. These models give a range of extinctions, stellar masses, and SFRs: $E(B-V) < 0.94$, $M_{\mathrm{stellar}} = [3.5 \pm 2.4] \times 10^{10}$ M$_\odot$, and SFR < 2000 $M_\odot$ yr^{-1} (Table 3). The dust-absorbed UV/optical luminosity range from 0% to 140% of the observed L_{8-1000}; but 90% of the models have dust-absorbed luminosity less than 50% of the observed L_{8-1000}.

We fit the far-IR SED with a single-temperature modified blackbody,

$$S(\nu_{\mathrm{obs}}) = \sigma \, (1 - e^{-\tau}) \, B(\nu_{\mathrm{rest}}, T) \, (1+z) \, \mu / d_L^2 \qquad (3)$$

where σ is the total absorption cross section of dust particles at the optically thick limit (i.e., the size of the dust-obscured region), $B(\nu, T)$ the *Planck* function, $\tau = (\nu_{\mathrm{rest}}/\nu_0)^\beta = (\lambda_0/\lambda_{\mathrm{rest}})^\beta$ the optical depth, μ the lensing magnification factor, and d_L the luminosity distance. In the optically thin limit ($\lambda \gg \lambda_0$), dust mass can be derived based on the knowledge of the opacity κ_d (absorption cross section per unit mass):

$$M_{\mathrm{dust}} = \frac{S(\nu_{\mathrm{obs}}) \, d_L^2}{\kappa_d(\nu_{\mathrm{rest}}) \, B(\nu_{\mathrm{rest}}, T) \, (1+z) \, \mu} \qquad (4)$$

It is generally assumed that the opacity follows a power law, $\kappa_d(\nu) \propto \nu^\beta$, and has a normalization of $\kappa_d = 0.07 \pm 0.02$ m^2 kg^{-1} at 850 μm (Dunne et al. 2000; James et al. 2002). Both the general "optically thick" ($S_\nu \propto (1 - e^{-\tau}) B_\nu(T)$) and the optically thin ($S_\nu \propto \nu^\beta B_\nu(T)$) models provide good fits to the observed SED (Fig. 4b). For the general model, we use all of the nine detections between 100 μm and 3 mm. The best-fit general model gives $\chi^2 = 1.6$ for dof = 5, suggesting that the photometric errors have been overestimated. For the optically thin model, we exclude the PACS 100 μm point, which is clearly on the Wien tail where small grains tend to dominate the emission. The best-fit optically thin model gives $\chi^2 = 4.0$ for dof = 5. The derived parameters are listed in Table 3.

The optically thick model yields dust properties similar to those of the local Ultra-Luminous Infrared Galaxy (ULIRG) Arp 220 (Rangwala et al. 2011), with the optical depth exceeds unity below rest-frame ~ 250 μm. The intrinsic $8-1000$ μm luminosity of $L_{8-1000} = [1.7 \pm 0.3] \times 10^{13}$ L$_\odot$ classifies HATLAS12−00 as a hyper-luminous infrared galaxy (Hy-LIRG). The IR luminosity implies an SFR of 1900 ± 400 M$_\odot$ yr^{-1} for a Chabrier (2003) IMF (Kennicutt 1998). Using the values of L_{8-1000} and $T = 63 \pm 2$ K in the Stefan-Boltzmann law we obtain a spherical source radius of 780 ± 100 pc, which is three times larger than that of Arp 220 (230 pc) because of the ten times greater luminosity. The source radius is comparable to that we derive from the optically thick model ($r = 500 \pm 60$ pc) and is consistent with the size we measure from modeling the SMA image (FWHM = $1.2^{+1.0}_{-0.5}$ kpc; § 3.3). Therefore, the optically thick model is preferred.

The radio luminosity from the observed 1.4 GHz flux density is $L_{1.4\mathrm{GHz}} = 4\pi d_L^2 S_{1.4\mathrm{GHz}}(1+z)^{\alpha-1} = [7.3 \pm 3.4] \times 10^{25}$ W Hz^{-1} for a radio spectral index of $\alpha = 0.7$. Assuming the radio emission is magnified by the same factor as the submillimeter emission, the IR-to-radio luminosity ratio of

HATLAS12−00, $q_L = \log(L_{\mathrm{IR}}/(4.52\mathrm{THz}\, L_{1.4\mathrm{GHz}})) = 2.1 \pm 0.2$, is consistent with the radio–far-IR correlation of high-redshift starburst galaxies: e.g., Kovács et al. (2006) measured $q_L = 2.14 \pm 0.12$ for 15 SMGs, while Ivison et al. (2010a) measured $q_L = 2.40 \pm 0.24$ for 65 *Herschel* 250 μm selected galaxies. This suggests that the AGN contribution is insignificant in HATLAS12−00.

We also do not see significant AGN contribution in the mid-IR. In Fig. 4b, we fit the SEDs of the local ULIRGs Mrk 231, Arp 220, and the $z = 2.3$ SMG "Cosmic Eyelash" (Ivison et al. 2010c) to the far-IR SED. The *WISE* upper limits lie well below the AGN-dominated ULIRG Mrk 231 but are more consistent with Arp 220 and the Eyelash. Therefore, we conclude that HATLAS12−00 is predominantly a starburst system.

5. DISCUSSION AND CONCLUSIONS

We have presented high-resolution K-band, 880 μm, and CO(1→0) observations and the near-IR-to-centimeter SED of a *Herschel*-selected strongly lensed SMG at $z = 3.2592$ (HATLAS12−00). The SMG shows distinctly different morphologies in the three images, suggesting differential magnification due to stratified morphologies. A joint strong lens modeling shows that the SMG is lensed by four galaxies at $z \sim 1$ and the luminosity-weighted magnification factors are 16.7 ± 0.8 in K, 7.6 ± 1.5 at 880 μm, and 6.9 ± 1.6 at CO(1→0). In the source plane, the SMG consists of several stellar clumps extended over ~ 1.6 kpc with $[3.5 \pm 2.4] \times 10^{10}$ M$_\odot$ of stars, a compact (~ 1 kpc) starburst enshrouded by $[7.0 \pm 2.0] \times 10^8$ of dust at ~ 60 K, and an extended (~ 6 kpc) cold molecular gas reservoir with $[7.4 \pm 2.1] \times 10^{10}$ M$_\odot$ of gas. The starburst and its gas reservoir are located ~ 4 kpc from the stars. Similar separations between optical and submillimeter/radio emission have been observed in unlensed high-redshift dusty starbursts (e.g., Tacconi et al. 2008; Casey et al. 2009; Bothwell et al. 2010; Carilli et al. 2010; Riechers et al. 2010). However, these previous results could also be attributed to astrometry offsets across different facilities; Casey et al. (2009) might be the only exception, whose tied the astrometry of the images to larger radio and optical fields. In HATLAS12−00, the physical separations amongst stars, dust, and gas are less ambiguous because of the clear wavelength-dependent morphologies in the image plane: fortuitously, the stars and dust/gas straddle across the caustic, so the less obscured K-band region is quadruply imaged while the heavily obscured starburst and its gas reservoir are doubly imaged. Because of the ~ 4 kpc separation between the stars and the gas-rich starburst and their similar masses, it is tempting to suggest that the SMG is in the process of a major merger, which presumably is driving the starburst activity in $z > 2$ SMGs (e.g., Tacconi et al. 2008; Engel et al. 2010). However, spatial separation of this scale can also be explained by differential dust obscuration in a single galaxy, as has been proposed for other high-redshift SMGs where spatial offsets have been observed between rest-frame UV and submillimeter (e.g., GN20 and AzTEC 3; Carilli et al. 2010; Riechers et al. 2010).

Differential magnification may affect the observed far-IR SED as well as the CO ladder, as hotter dust and higher-J CO lines may have more compact morphologies (Ivison et al. 2011). However, because the magnification map is smooth in the area, the six times difference in the sizes of the CO(1→0) and the dust emitting region only lead to a $\sim 10\%$ difference in magnification, which is smaller than the 1σ errors of our estimates of the magnification factors. Therefore, differen-

tial magnification is unlikely to be significant enough to affect the far-IR SED and future CO ladder measurements in HATLAS12−00.

How does the massive gaseous disk compare with the disks in other SMGs? We estimate an dynamical mass of $[3.2 \pm 1.3] \times 10^{11}$ M$_\odot$ and a gas fraction of $f_{gas} = M_{gas}/M_{dyn} = 23 \pm 11\%$ for the CO(1→0) disk using the "isotropic virial estimator" (e.g., Tacconi et al. 2008):

$$M_{dyn} = 2.8 \times 10^5 \Delta V_{FWHM}^2 r_{HWHM} \; M_\odot, \qquad (5)$$

where ΔV_{FWHM} is the CO line FWHM in km s^{-1} and r_{HWHM} is half of the FWHM size of the disk in kpc. Combined with the FWHM disk radius, we further estimate a gas surface density of $\Sigma = 510 \pm 370$ M$_\odot$ pc^{-2}. Both f_{gas} and Σ are similar to those of the extended CO(1→0) disks in the two $z \sim 3.4$ SMGs in Riechers et al. (2011b). But both values are significantly smaller than those of the kinematically resolved CO(6→5) disk of the "Cosmic Eyelash" ($f_{gas} \sim 70\%$, $\Sigma \sim 3000 \pm 500$ M$_\odot$ pc^{-2}; Swinbank et al. 2011). The discrepancies illustrate the limitations of these widely used but crude estimators *and/or* that high excitation CO lines probe more compact and denser regions in a disk. Higher resolution observations are clearly needed to resolve this issue. Without spatially resolved gas kinematics, we refrain from estimating the disk stability parameter of Toomre (1964).

HATLAS12−00 is a gas-rich, initial starburst system similar to unlensed SMGs and local ULIRGs. Its intrinsic IR luminosity well exceeds 10^{13} L$_\odot$ (i.e., Hy-LIRG), implying an enormous rate of star formation (1900 ± 400 M$_\odot$ yr^{-1}). Although the molecular gas reservoir is massive and it constitutes $68 \pm 17\%$ of the *visible* baryonic mass ($M_{gas} + M_{dust} + M_{stellar}$) and $23 \pm 11\%$ of the dynamical mass, it will exhaust in just 39 ± 14 ($\alpha_{CO}/0.8$) Myr at the current SFR (assuming no gas accretion). The star formation timescale, $\tau_{SF} = M_{stellar}/\mathrm{SFR} = 18 \pm 13$ Myr, is only $\sim 1\%$ of the cosmic age at $z = 3.2592$ ($\tau_{cosmic} = 1.9$ Gyr), suggesting that HATLAS12−00 is an initial starburst system with maturity $\mu = \tau_{SF}/\tau_{cosmic} \ll 1$ (Scoville et al. 2007). The specific SFR, sSFR = SFR/$M_{stellar}$ $= 54 \pm 38$ Gyr^{-1}, is consistent with the average $z > 2$ SMGs, but it is an order of magnitude higher than the median value of the star-forming main sequence of Lyman break galaxies at the same epoch (Daddi et al. 2009). We can also estimate the star formation efficiency: $\epsilon = t_{dyn}/(M_{gas}/\mathrm{SFR})$, where $t_{dyn} = \sqrt{r^3/(2GM)}$ is the dynamical or free-fall timescale. For $r = r_{HWHM} = 3$ kpc and $M = M_{dyn}$, we obtain $\epsilon = 0.11 \pm 0.04$, or $[11 \pm 4]\%$ per dynamical timescale, which is comparable to unlensed SMGs but is an order of magnitude higher than normal starforming galaxies (Genzel et al. 2010).

The dust mass of $[7.0 \pm 2.0] \times 10^8$ M$_\odot$ is similar to the average dust mass of unlensed SMGs (e.g., Michalowski et al. 2010), and the gas-to-dust ratio, $M_{gas}/M_{dust} = 110 \pm 40$ ($\kappa_{850\mu m}/0.07$ m^2 kg^{-1}) ($\alpha_{CO}/0.8$), is comparable to that of the Milky Way. Assuming that the dust emission is indicative of the size of the starburst and a starburst disk radius of $r_0 = 1$ kpc, the star formation surface density of $\dot{\Sigma}_\star \simeq 600 \pm 120$ $M_\odot$ yr^{-1} kpc^{-2} approaches the Eddington limit of radiation pressure supported starburst disks ($\dot{\Sigma}_\star \sim 10^3$ $M_\odot$ yr^{-1} kpc^{-2}; Scoville 2003; Thompson et al. 2005), similar to local ULIRGs such as Arp 220 and the host galaxy of the $z = 6.4$ quasar SDSS J114816.64+525150.3 (Walter et al.

2009).

In conclusion, HATLAS12−00 is a *bona fide* SMG with an intrinsic submillimeter flux density of $S_{880} = 9.2 \pm 2.2$ mJy. The starburst disk, where most of the molecular gas and dust reside, is spatially separated from the less obscured stellar population by ~ 4 kpc, suggesting either a major merger or differentiated dust obscuration. The ~ 1 kpc radius starburst disk is presumably supported in large by radiation pressure on the dust grains. Its physical properties, such as molecular gas mass, stellar mass, gas-to-dust ratio, gas fraction, SFR, star formation efficiency, and radio-to-far-IR luminosity ratio, are all very similar to unlensed $z > 2$ SMGs (Hainline et al. 2011; Wardlow et al. 2011; Michalowski et al. 2010; Kovács et al. 2006). The lensing boost of the effective angular resolution and sensitivity has allowed us to examine in unprecedented details the properties of a typical starburst galaxy when the Universe is only 1/7 of its current age. HATLAS12−00 provides a prelude to a golden age of SMG research, as *Herschel* is unveiling hundreds of strongly lensed SMGs before the mission completes (e.g., González-Nuevo et al. 2012, Wardlow et al. in prep).

REFERENCES

Aihara, H., et al. 2011, ApJS, 193, 29
Aravena, M., et al. 2010, ApJ, 708, L36
Becker, R. H., White, R. L., & Helfand, D. J. 1995, ApJ, 450, 559
Benn, C., Dee, K., & Agócs, T. 2008, in SPIE Conference Series, Vol. 7014, 229
Blain, A. W. 1996, MNRAS, 283, 1340
Blain, A. W., Smail, I., Ivison, R. J., Kneib, J. P., & Frayer, D. T. 2002, Physics Reports, 369, 111
Bock, D. C. J., et al. 2006, in SPIE Conference Series, Vol. 6267, 36
Bothwell, M. S., et al. 2010, Monthly Notices of the Royal Astronomical Society, 405, 219
Brammer, G. B., van Dokkum, P. G., & Coppi, P. 2008, ApJ, 686, 1503
Bruzual, G., & Charlot, S. 2003, MNRAS, 344, 1000
Bussmann, R. S., et al. 2012, ApJ, submitted
Calzetti, D., Kinney, A. L., & Storchi-Bergmann, T. 1994, ApJ, 429, 582
Carilli, C. L., et al. 2010, ApJ, 714, 1407
Casey, C. M., et al. 2009, MNRAS, 399, 121
Chabrier, G. 2003, PASP, 115, 763
Chapman, S. C., Blain, A. W., Smail, I., & Ivison, R. J. 2005, ApJ, 622, 772
Combes, F., et al. 2012, arXiv:1201.2908
Conley, A., et al. 2011, ApJ, 732, L35
Cox, P., et al. 2011, ApJ, 740, 63
da Cunha, E., Charlot, S., & Elbaz, D. 2008, MNRAS, 388, 1595
Daddi, E., et al. 2009, ApJ, 694, 1517
Dannerbauer, H., Lehnert, M. D., Lutz, D., Tacconi, L., Bertoldi, F., Carilli, C., Genzel, R., & Menten, K. M. 2004, ApJ, 606, 664
Dunne, L., Eales, S., Edmunds, M., Ivison, R., Alexander, P., & Clements, D. L. 2000, MNRAS, 315, 115
Eales, S., et al. 2010, PASP, 122, 499
Eddington, A. S. 1913, MNRAS, 73, 359
Engel, H., et al. 2010, ApJ, 724, 233
Frayer, D. T., et al. 2004, ApJS, 154, 137
Genzel, R., et al. 2010, MNRAS, 1296
González-Nuevo, J., et al. 2012, ApJ, in press, arXiv:1202.0402
Hainline, L. J., Blain, A. W., Smail, I., Alexander, D. M., Armus, L., Chapman, S. C., & Ivison, R. J. 2011, ApJ, 740, 96
Harris, A. I., et al. 2012, ApJ, in press, arXiv:1204.4706
Herranz, D., et al. 2012, A&A, submitted, arXiv:1204.3917
Hickox, R. C., et al. 2012, MNRAS, 421, 284
Ibar, E., et al. 2010, MNRAS, 409, 38
Ivezić, Ž., et al. 2002, AJ, 124, 2364
Ivison, R. J., et al. 2010a, A&A, 518
Ivison, R. J., Papadopoulos, P. P., Smail, I., Greve, T. R., Thomson, A. P., Xilouris, E. M., & Chapman, S. C. 2011, MNRAS, 412, 1913
Ivison, R. J., Smail, I., Papadopoulos, P. P., Wold, I., Richard, J., Swinbank, A. M., Kneib, J. P., & Owen, F. N. 2010b, MNRAS, 404, 198
Ivison, R. J., et al. 2010c, A&A, 518, L35
James, A., Dunne, L., Eales, S., & Edmunds, M. G. 2002, MNRAS, 335, 753
Jeffreys, H. 1961, Theory of probability. (Oxford: Clarendon Press)
Jullo, E., Kneib, J. P., Limousin, M., Elíasdóttir, Á., Marshall, P. J., & Verdugo, T. 2007, New Journal of Physics, 9, 447
Kassiola, A., & Kovner, I. 1993, ApJ, 417, 450
Kennicutt, Robert C., J. 1998, ARA&A, 36, 189
Kneib, J. P., Ellis, R. S., Smail, I., Couch, W. J., & Sharples, R. M. 1996, ApJ, 471, 643
Kochanek, C. S., & Narayan, R. 1992, ApJ, 401, 461
Kormann, R., Schneider, P., & Bartelmann, M. 1994, A&A, 284, 285

Kovács, A., Chapman, S. C., Dowell, C. D., Blain, A. W., Ivison, R. J., Smail, I., & Phillips, T. G. 2006, ApJ, 650, 592
Kreysa, E., et al. 1999, Infrared Physics and Technology, 40, 191
Lapi, A., et al. 2011, ApJ, 742, 24
Lawrence, A., et al. 2007, MNRAS, 379, 1599
Lilly, S. J., Eales, S. A., Gear, W. K. P., Hammer, F., Le Fèvre, O., Crampton, D., Bond, J. R., & Dunne, L. 1999, ApJ, 518, 641
Michalowski, M. J., Watson, D., & Hjorth, J. 2010, ApJ, 712, 942
Morton, D. C., & Noreau, L. 1994, ApJS, 95, 301
Narayanan, D., Krumholz, M. R., Ostriker, E. C., & Hernquist, L. 2012, MNRAS, 421, 3127
Negrello, M., González-Nuevo, J., Magliocchetti, M., Moscardini, L., De Zotti, G., Toffolatti, L., & Danese, L. 2005, MNRAS, 358, 869
Negrello, M., et al. 2010, Science, 330, 800
Negrello, M., Perrotta, F., González-Nuevo, J., Silva, L., de Zotti, G., Granato, G. L., Baccigalupi, C., & Danese, L. 2007, MNRAS, 377, 1557
Pascale, E., et al. 2011, MNRAS, 415, 911
Peng, C. Y., Ho, L. C., Impey, C. D., & Rix, H.-W. 2010, AJ, 139, 2097
Perley, R. A., Chandler, C. J., Butler, B. J., & Wrobel, J. M. 2011, ApJ, 739, L1
Pilbratt, G. L., et al. 2010, A&A, 518, L1
Planck Collaboration. 2011a, A&A, 536, 1
—. 2011b, A&A, 536, 7
Press, W. H., Teukolsky, S. A., Vetterling, W. T., & Flannery, B. P. 1992, Numerical recipes in C. The art of scientific computing (Cambridge: University Press, |c1992, 2nd ed.)
Rangwala, N., et al. 2011, ApJ, 743, 94
Renzini, A. 2006, ARA&A, 44, 141
Riechers, D. A., et al. 2010, ApJ, 720, L131
—. 2011a, ApJ, 733, L12
Riechers, D. A., Hodge, J., Walter, F., Carilli, C. L., & Bertoldi, F. 2011b, ApJ, 739, L31
Rigby, E. E., et al. 2011, MNRAS, 415, 2336
Sault, R. J., Teuben, P. J., & Wright, M. C. H. 1995, in ASPC, Vol. 77
Scott, K. S., et al. 2011, ApJ, 733, 29
Scoville, N. 2003, Journal of Korean Astronomical Society, 36, 167
Scoville, N., et al. 2007, ApJS, 172, 150
Siringo, G., et al. 2009, A&A, 497, 945
Sluse, D., Chantry, V., Magain, P., Courbin, F., & Meylan, G. 2011, arXiv:1112:0005
Solomon, P. M., & Vanden Bout, P. A. 2005, ARA&A, 43, 677
Swinbank, A. M., Chapman, S. C., Smail, I., Lindner, C., Borys, C., Blain, A. W., Ivison, R. J., & Lewis, G. F. 2006, MNRAS, 371, 465
Swinbank, A. M., et al. 2011, ApJ, 742, 11
Tacconi, L. J., et al. 2008, ApJ, 680, 246
Thompson, T. A., Quataert, E., & Murray, N. 2005, ApJ, 630, 167
Toomre, A. 1964, ApJ, 139, 1217
Vieira, J. D., et al. 2010, The Astrophysical Journal, 719, 763
Walter, F., Riechers, D., Cox, P., Neri, R., Carilli, C., Bertoldi, F., Weiss, A., & Maiolino, R. 2009, Nature, 457, 699
Wardlow, J. L., et al. 2011, MNRAS, 415, 1479
Wizinowich, P. L., et al. 2006, PASP, 118, 297
Wright, E. L., et al. 2010, AJ, 140, 1868
Wucknitz, O. 2004, MNRAS, 349, 1